# Supporting Information

## Horowitz et al. 10.1073/pnas.1211311109

### SI Text

**Nanodiamond Samples.** Fig. S1 shows electron microscopy images of the nanodiamonds. These particles are synthetic high-pressure high-temperature type Ib diamond, approximately 100 nm in size, and irradiated with $He^+$ ions to create vacancies and annealed. The resulting product is purified using acids. The nanodiamonds are specified by the manufacturer (Adámas Nanotechnologies) to contain on average >500 NV centers/particle. We also used 0–0.2 μm nanodiamonds from Microdiamant that are not irradiated or annealed in some of the measurements in this *SI Text*.

**Fluorescence Spectrum.** A fluorescence spectrum of optically trapped nanodiamonds is shown in Fig. S2. A significant portion of the signal, 42%, is lost due to the optical tweezers dichroic filter. One improvement to the collection efficiency would be to replace this dichroic with one that transmits rather than reflects wavelengths from 700 nm to 800 nm.

**Apparatus and Techniques.** Fig. S3 shows a schematic of the optical apparatus. A 5 W continuous wave 1,064 nm laser (NP Photonics seed laser and PM-ASA-SFA-5W amplifier, Nufern) optically traps nanodiamonds in solution in water. A 100 mW continuous wave 532 nm laser (GCL-532-100-L CW DPSS, CrystaLaser) excites photoluminescence and polarizes the NV spin into the $m_s = 0$ spin state. A holographic laser bandpass filter (Kaiser Optical Systems, Inc.) removes excess wavelengths from the 532 nm excitation laser. The infrared and green lasers are attenuated to 30 mW and 90 μW, respectively, with the exception of Fig. 4*A*, for which the green excitation laser was attenuated to 50 μW, measured at the back opening of the objective in each case. The photoluminescence signal is detected by an avalanche photodiode single photon counting module (SPCM-AQRH-13-FC, Perkin Elmer) whose pulses are counted by a data acquisition instrument (National Instruments). The 1,064 nm and 532 nm beams are combined using dichroic mirrors (Chroma) mounted in a pair of dichroic turrets built into an inverted microscope (TE2000U, Nikon). An oil-immersion objective (CFI Plan Fluor 100×, Nikon) with numerical aperture 1.3 focuses the beams onto the sample. We mount the sample on a three-axis piezoelectric stage (P-517.3CL with E-710.4CL controller, Physik Instrumente), which enables moving the antenna/coverslip assembly by up to 100 microns in X and Y and up to 20 microns in Z. We calibrate the electromagnet (EM050-6H-222, APW Company) with a Hall probe (HMMA-1808-VR probe and 455 DSP Gaussmeter, Lakeshore). A Hewlett Packard ESG-D4000A generates the microwave signal, which is amplified by an Amplifier Research 5S1G4. The fluorescence spectrum is measured with a SpectraPro 2750 spectrometer (PI Acton). A 92/8 pellicle beam-splitter directs a fraction of the optical signal to a color camera (PL-B681CF-KIT, PixeLINK). The optical signal is filtered with a 640 nm long pass filter and a 1,064 nm notch block filter to remove laser scatter prior to photon detection by avalanche photodiode. All optical measurements were taken with room lights off to avoid extra photon counts.

The antenna/coverslip assembly is shown in Fig. S4*A*. The antenna is impedance matched to 50 Ω. The design was developed using COMSOL Multiphysics simulations. The magnetic flux density in the vicinity of the antenna resulting from a microwave field is shown in Fig. S4 *B* and *C*.

The software lock-in is shown in Fig. S5 *A* and *B*. Since $f_{MW}$ is resonant with the energy splitting between the $m_s = 0$ and the $m_s = +1$ or $-1$ states, $I_{PL}$ drops while the microwave is on, such that $I_{PL}$ oscillates in time at frequency $f_{AM}$. Locking in to the signal, we extract the differential fluorescence signal $\Delta I_{PL}$. As we sweep the microwave frequency $f_{MW}$, $\Delta I_{PL}$ remains low when $f_{MW}$ is off resonance with the transition between spin states and increases when $f_{MW}$ is on resonance. If $X$ and $Y$ are the two output channels of the lock-in, and $R = \sqrt{X^2 + Y^2}$, then $\Delta I_{PL} = 2R$. Fig. S5*C* shows the ESR spectrum for an ensemble of trapped nanodiamonds in water with no externally applied magnetic field. The nanodiamonds are specified to be 100 nm in diameter and contain 500 NV centers each. The spectrum has a linewidth of 23.6 MHz and a maximum at 2.87 GHz, agreeing with the expected zero-field splitting of the NV center. Off resonance, the curve does not go to zero because the lock-in is not phase locked.

**$I_{PL}$-Dependence of Noise.** The photoluminescence noise from optically trapped fluorescent nanodiamonds shows a dependence on the photoluminescence, $I_{PL}$. In general, the standard deviation of the experimentally measured $I_{PL}$, $\sigma_{expt}$, grows with increased $I_{PL}$ beyond that expected from Poisson statistics or shot noise behavior, namely $\sigma_{expt} > \sigma_{shot} = \sqrt{N}$, where $N = I_{PL}\Delta t$, and $\Delta t$ is the time interval in which photon counts are measured. Fig. S6 illustrates this dependence and plots the ratio $\sigma_{expt}/\sqrt{N}$ as a function of $I_{PL}$. For low values of $I_{PL}$, $\sigma_{expt}$ approaches shot noise (dotted line in Fig. S6), but reaches values nearly six times shot noise at higher $I_{PL}$. Analysis of noise is performed only on plateaus with stable $I_{PL}$, therefore the plotted noise, especially for higher $I_{PL}$, is a lower limit. As discussed in the text, this increase in noise likely arises from dynamics of multiple particles in the trap. Any motion of particles in the trap, arising from collisions, thermal vibrations, trap instability, etc., will have a corresponding contribution to the noise in $I_{PL}$ because each particle will experience a varying degree of electric field strength from the laser beam determined by its position in the measurement volume. In addition, when a fluorescent particle enters the trap, the abrupt increase in $I_{PL}$ contributes to the noise.

**Measurements of Dry, Fixed Nanodiamonds.** In addition to measuring optically trapped nanodiamonds, we have also measured nanodiamonds stuck to the coverslip. Fig. S7 shows ESR of nanodiamonds that are drop-cast onto the coverslip. To mitigate the influence of non-NV-based fluorescence, we photobleach the sample with the 532 nm laser, intending to let only the nonphotobleaching NV fluorescence signal remain. The ESR signal splits into more than two peaks, indicating that the measurement ensemble includes multiple NV centers at different orientations. These nanodiamonds are not irradiated. We see more peaks in the ESR spectra of irradiated nanodiamonds when they are drop-cast onto the coverslip owing to the higher number of NV centers. We observe a higher signal-to-noise ratio for ESR spectra taken with stuck nanodiamonds than with optically trapped nanodiamonds. This suggests that trapping dynamics and a decreased optical collection efficiency contribute to the lower signal-to-noise ratio in optically trapped nanodiamonds.

**Modeling the ESR Spectrum.** The diamond nanoparticles in the trap are not expected to be aligned or oriented in any particular direction. In addition, the particles likely rotate in the optical trap. From the Einstein-Smoluchowski relation, we estimate the rotational diffusion constant of the nanodiamonds is 1.3 kHz at room temperature, so we expect that they are rotating many times while

each ESR data point is collected, averaging over all possible orientations. Therefore, we model the ESR spectrum by assuming the NV centers are randomly oriented. We begin by calculating the angular dependence of the excitation (i.e., absorption) and emission of a single NV center, then calculate the ESR peak frequencies as a function of magnetic field strength and NV center orientations. Next, we integrate the contributions of an isotropic density of NV center angles to obtain the predicted ESR spectra for a large ensemble of randomly oriented NV centers in a magnetic field aligned with the axis of the microscope objective. Finally, we use a Markov Chain Monte Carlo approach to fit the modeled curve to the data and to extract parameters such as the estimated magnetic field and the magnetic sensitivity.

***Angular dependence of the absorption of a single NV center.*** The absorption of a single transition dipole is proportional to $|\mathbf{p}\cdot\mathbf{E}|^2$, where $\mathbf{E}$ is the electric field vector of the exciting laser beam and $\mathbf{p}$ is the dipole, which we treat classically. An NV center has two transition dipoles, each perpendicular to the axis of the NV center (1), so the combined absorption is

$$\text{Absorption} \propto |\mathbf{p}_1\cdot\mathbf{E}|^2 + |\mathbf{p}_2\cdot\mathbf{E}|^2.$$

Although a highly focused Gaussian beam includes electric fields at multiple angles, we approximate that the electric field that excites the NV center is uniform and is perpendicular to the axis of the microscope objective. We also assume that the electric field is linearly polarized, $\mathbf{E}_{\text{laser}} = E_x\hat{x}$, though this assumption is merely for convenience and will not affect the calculation once the absorption is integrated over all possible NV angles. The laser polarization would be important if the magnetic field were applied along a different axis with respect to the microscope objective, but our geometry has a symmetry so the polarization of the laser is not important. Laser polarization control could provide a route to vector magnetometry using an ensemble of randomly oriented NV centers.

For a given NV center with an angle θ with respect to the axis of the microscope objective, we can specify with no loss of generality that its dipole $\mathbf{p}_1$ is perpendicular to the axis of the microscope objective. Then $\mathbf{p}_2$ must be perpendicular to $\mathbf{p}_1$. It is convenient to define these vector directions using a cross product:

$$\frac{\mathbf{p}_1}{|\mathbf{p}_1|} = \frac{\hat{N}\times\hat{z}}{|\hat{N}\times\hat{z}|} \quad \text{and} \quad \frac{\mathbf{p}_2}{|\mathbf{p}_2|} = \frac{\hat{N}\times\mathbf{p}_1}{|\hat{N}\times\mathbf{p}_1|},$$

where $\hat{z}$ points along the axis of the microscope objective and $\hat{N}$ is a unit vector pointing along the direction of the symmetry axis of the NV center,

$$\hat{N} = \sin\theta\cos\phi\hat{x} + \sin\theta\sin\phi\hat{y} + \cos\theta\hat{z},$$

where θ is the polar angle and $\phi$ is the azimuthal angle. By symmetry, $|\mathbf{p}_1| = |\mathbf{p}_2|$. Then the angular dependence of the absorption of a single NV center is $1-\cos^2\phi\sin^2\theta$. Integrating over all $\phi$, we obtain

$$\text{Absorption} \propto 1+\cos^2\theta. \qquad \textbf{[S1]}$$

We will integrate over all angles θ at a later point in the calculation.

***The emission collected from a single NV center.*** In order to calculate the collected emission of the transition dipole, we begin by calculating the angular part of the emission function of a dipole $\mathbf{p}$, which we treat classically. The component of the dipole that is orthogonal to the direction vector $\hat{r}$ is

$$\mathbf{p}_\perp = \mathbf{p} - \hat{r}(\hat{r}\cdot\mathbf{p}),$$

where

$$\hat{r} = \sin\vartheta\cos\varphi\hat{x} + \sin\vartheta\sin\varphi\hat{y} + \cos\vartheta\hat{z}.$$

The power radiated by the dipole is proportional to $|\mathbf{p}_\perp|^2$. We integrate over the collection cone of the microscope objective to find the angular part of the power collected,

$$P_1 \propto \int_0^{\vartheta_{\max}}\int_0^{2\pi} |\mathbf{p}_\perp|^2 \sin\vartheta d\varphi d\vartheta$$

where $P_1$ is the collected emission of one dipole and $\vartheta_{\max}$ is the maximum angle at which the objective can collect light; because $\text{NA} = n\sin\vartheta_{\max}$ with $n = 1.515$ and $\text{NA} = 1.3$, we have $\vartheta_{\max} = 59.1°$. We assume that the objective has uniform efficiency for collecting light from all angles in its collection cone. An objective with a lower NA would have a stronger angular dependence of the collection. The result is

$$P_1 \propto 2.43(p_x^2+p_y^2) + 1.25p_z^2,$$

where $p_x$, $p_y$, and $p_z$ are the components of $\mathbf{p}$. If we account for the geometry of the two transition dipoles of the NV center, and let θ be the angle between the NV center and the axis of the microscope objective, then the collected radiation of the dipoles $\mathbf{p}_1$ and $\mathbf{p}_2$ depends on the orientation of the NV center according to

$$\text{Collected emission} \propto 2.43 + 2.43\cos^2\theta + 1.25\sin^2\theta. \qquad \textbf{[S2]}$$

***Zeeman splitting.*** The energy levels of the spin states of the ground state of the NV center are calculated directly from the ground state Hamiltonian,

$$\hat{H}_{\text{NV}} = D\hat{S}_z^2 + g\mu_B\mathbf{B}\cdot\hat{\mathbf{S}},$$

where $D = h\cdot 2.87$ GHz, $g = 2.00$, $\mu_B$ is the Bohr magneton, and the components of $\hat{\mathbf{S}}$ are the spin 1 matrices. Terms of the Hamiltonian not relevant to this calculation have been suppressed. The difference between spin levels gives the frequency of the peaks measured in the ESR spectrum of a single NV center. That is, for a given field $\mathbf{B}$, the spectrum will have peaks corresponding to

$$hf_{0\to+1} = E_{m_s=+1} - E_{m_s=0} \quad \text{and} \quad hf_{0\to-1} = E_{m_s=-1} - E_{m_s=0},$$

where $E_{m_s=0}$, $E_{m_s=-1}$, and $E_{m_s=+1}$ are the three eigenvalues of $\hat{H}_{\text{NV}}$. Fig. S8*A* shows how these spin sublevel frequencies depend on the angle of the NV center to the magnetic field. For zero field, $E_{m_s=-1} = E_{m_s=+1}$, so the peaks are degenerate, $hf_{0\to-1} = hf_{0\to+1} = D$. The frequencies split with magnetic field. For NV centers aligned with the magnetic field, and for fields below 1,000 G, the frequencies are linear in the magnetic field: $hf_{0\to\pm1}(\theta=0) = D \pm g\mu_B B$, where $g\mu_B/h = 2.80$ MHz/G and θ is the angle between the NV axis and the magnetic field vector. However, the frequency $f_{0\to-1}$ varies more with θ than $f_{0\to+1}$ does, causing an asymmetry at nonzero fields.

***ESR spectrum of a single NV center.*** We assume that each NV center in the distribution has an ESR spectrum with two Gaussian functions, one peak centered at $f_{0\to-1}$ and the other at $f_{0\to+1}$. These frequencies depend on the magnetic field strength and the angle θ between the magnet and the axis of the NV center. Note that for our geometry, where the magnet and the objective share an axis (see Fig. 1*A* or Fig. S3), this is the same angle as the angle between the NV center and the axis of the microscope objective; for the purposes of the calculation, we assume no misalignment between the magnet and the microscope objective. We ignore the effects of spin-mixing that cause $I_{\text{PL}}$ to decrease in a magnetic

field (1, 2), which should be small for fields ranging from 0 to 100 G. The amplitude of this double-Gaussian single-NV ESR spectrum depends on the angle θ between the axis of the NV center and the axis of the microscope objective:

$$A_1(\theta) \propto (1 + \cos^2\theta)(2.43 + 2.43\cos^2\theta + 1.25\sin^2\theta), \quad \textbf{[S3]}$$

where Eqs. **S1** and **S2** give the angular dependence of the absorption and collected emission of the NV center. Note that the NV center can emit a photon via either dipole, regardless of the dipole that absorbed a photon. We approximate that the microwave power affects the NV centers uniformly. Therefore the ESR spectrum $C_1(B, \theta; f_{\mathrm{MW}})$ of a single NV has angular dependence

$$C_1(B, \theta; f_{\mathrm{MW}}) = A_1(\theta)[G(f_{0\to+1}; f_{\mathrm{MW}}) + G(f_{0\to-1}; f_{\mathrm{MW}})],$$

where $G(x_0; x)$ is a Gaussian function of $x$ centered at $x_0$, and $f_{0\to+1}$ and $f_{0\to-1}$ are functions of $B$ and θ as shown in Fig. S8*A*. The widths of the two Gaussian functions must be determined empirically and are assumed to be equal to each other.

***ESR spectrum of an isotropic ensemble of NV centers.*** To obtain the ESR spectrum of an ensemble of NV centers, $C_{\mathrm{model}}(B, f_{\mathrm{MW}})$, we integrate over all angles θ,

$$C_{\mathrm{model}}(B, f_{\mathrm{MW}}) = \int_0^{\pi} C_1(B, \theta; f_{\mathrm{MW}}) \sin\theta d\theta, \quad \textbf{[S4]}$$

and the result is plotted in Fig. S8*B*. Note that for an isotropic distribution of NV centers, more NV centers will be perpendicular to the axis of the magnet/objective than parallel to this axis, with a probability distribution given by $\sin\theta$. The model predicts two peaks separating and broadening as the magnetic field is increased. The right peak is predicted to be taller and narrower than the left peak because of the asymmetry between $f_{0\to-1}$ and $f_{0\to+1}$.

***Fitting the ESR curves.*** To compute marginal posterior densities for the sensitivities and infer the magnetic field experienced by the NV centers in the main text, we employ the MT-DREAM$_{\mathrm{ZS}}$ algorithm written in MATLAB (3, 4), a Markov Chain Monte Carlo approach that uses adaptive proposal distribution tuning, multiple-try sampling, sampling from the past, and snooker update on parallel chains to rapidly explore high-dimensional posterior distributions. In Markov Chain Monte Carlo, each of the $N$ chains executes a random walk through the parameter space following a modified Metropolis-Hastings rule to control whether a proposed $d$-dimensional move is accepted or rejected. Because the algorithm is ergodic and maintains detailed balance at each step, the target distribution after a burn-in period is the desired posterior probability distribution for the experiment. We find good results using the recommended settings along with $N = 6$ parallel chains with multiple-try parameter $k = 3$. Although the dimensionality of the problem ($d = 6$) is low, in practice multiple-try sampling is advantageous for faster convergence and better autocorrelation properties of the sampler output. Because the model relies on the numerical convolution over the orientation angle of the NV centers, the evaluation of the posterior probability density and the estimates of its derivative can be slow to compute. We vectorized the computation of both the Hamiltonian eigenvalues and numerical integrations over θ for each modeled frequency curve and used an NVIDIA GTX-440 graphics processing unit along with MATLAB software package `Jacket` from Accelereyes to greatly increase the speed of computations of the posterior density. Convergence to the target distribution was assessed both graphically and with the Gelman-Rubin statistic, $\hat{R} < 1.02$ (5). The point estimates for the magnetic field ($B$), the homoscedastic normal error at each datapoint (σ), and other parameters are computed from the respective sample empirical means, and the highest probability density intervals are computed using the method of Chen and Shao (6).

The mean of the marginal posterior density of $B$ is plotted in Fig. S9*A*. The 95% highest probability density intervals are plotted as error bars. The plot demonstrates the ability of the apparatus to sense the applied calibrated magnetic field. The discrepancy between the applied field and measured field is about 5 G and appears to be a repeatable, constant offset. We attribute this error to the magnetic piezostage used in the experiment, whose field is not accounted for in the calibration. Another explanation may be some deficiency in the model, but the linearity of the sensed magnetic field versus applied magnetic field seems to discount this as the primary issue.

**Magnetic Sensitivity.** For theoretical sensitivity calculations, we consider the optimal measuring frequency to be the frequency at which the derivative $\frac{\partial C}{\partial B}$ has maximum magnitude. One can imagine constructing a measurement scheme for magnetometry that occurs at this single frequency to detect small changes in the applied magnetic field $B$. Having inferred the noise in the contrast of our measurement from the analysis, we use the 1σ change as the critical value for the minimum detectable change in magnetic field. Given the value of σ inferred from our experiments as a function of field, we calculate a theoretical sensitivity for such an idealized measurement (black circles in Fig. S9*B*). The computation proceeds by taking individual samples from the Markov Chain Monte Carlo output and computing the maximum magnitude of the partial derivative with respect to $B$ at each parameter space sample, and dividing the corresponding sample of σ by this numerical derivative to generate the posterior distribution of the sensitivity η. The heavy tails of η at zero field, which arise from the vanishing of the numerical derivative $\frac{\partial C}{\partial B}$ as $B$ tends to zero, explain the large error bars found there. As a practical check, we can estimate the achieved sensitivity of the magnetometer on the basis of a scheme of taking ESR sweeps in the same fashion taken in the main text. By computing the fitting uncertainty from the marginal distribution of $B$ and scaling it by the square root of the acquisition time, we can calculate an empirical measure of the instrument sensitivity, i.e. $\eta_{\mathrm{empirical}} = \sigma_B\sqrt{\Delta t}$. These calculated values are additionally plotted in Fig. S9*B* (open purple circles) for comparison to the theoretical values. In the empirical scheme, the microwave frequency is swept across the spin resonances but also measures the off-resonant signal that contributes almost no information to the determination of $B$. Thus, the empirical measure is necessarily less efficient in its use of the resource of acquisition time, with a commensurately worse sensitivity. The observation that the theoretical sensitivities proposed in the manuscript are only a few times better than the empirical sensitivities demonstrated directly from the fitting ensures that the theoretical estimates are not unreasonable.


1. Epstein RJ, Mendoza FM, Kato YK, Awschalom DD (2005) Anisotropic interactions of a single spin and dark-spin spectroscopy in diamond. *Nat Phys* 1:94–98.
2. Lai ND, Zheng D, Jelezko F, Treussart F, Roch JF (2009) Influence of a static magnetic field on the photoluminescence of an ensemble of nitrogen-vacancy color centers in a diamond single-crystal. *Appl Phys Lett* 95:133101.
3. Vrugt JA, Laloy E, ter Braak CJF, Hyman JM (2012) Posterior exploration using differential evolution adaptive metropolis with sampling from past states. To be submitted to *SIAM J Optim*.
4. Laloy E, Vrugt JA (2012) High-dimensional posterior exploration of hydrologic models using multiple-try DREAM$_{(\mathrm{zs})}$ and high-performance computing. *Water Resourc Res* 48:W01526.
5. Gelman A, Rubin DB (1992) Inference from iterative simulation using multiple sequences. *Statl Sci* 7:457–472.
6. Chen MH, Shao QM (1999) Monte Carlo estimation of Bayesian credible and HPD intervals. *J Comput Graph Stat* 8:69–92.

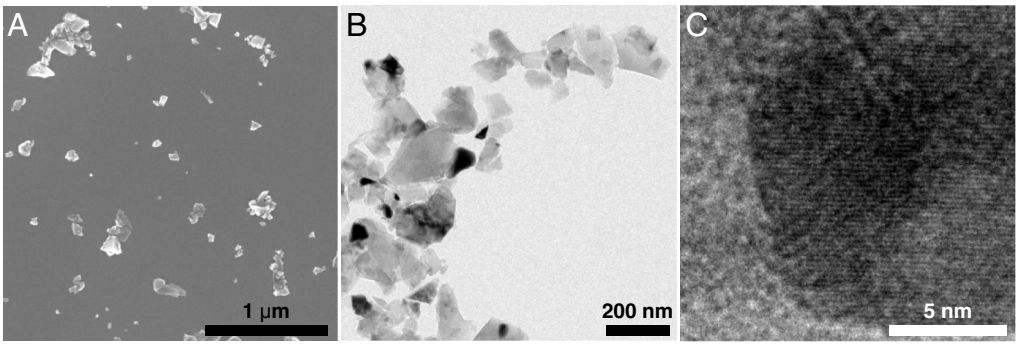


**Fig. S1.** (*A*) Scanning electron micrograph and (*B* and *C*) transmission electron micrograph of nanodiamonds (ND-500NV-100 nm, Adámas Nanotechnologies).

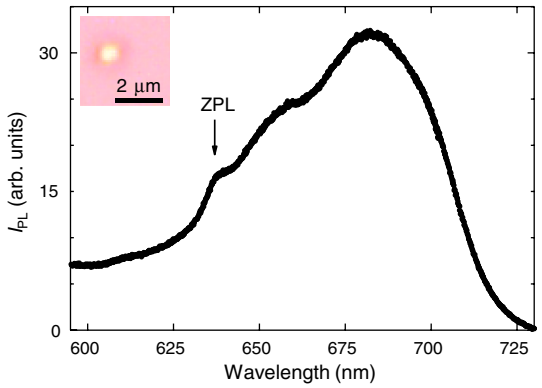


**Fig. S2.** Photoluminescence spectrum of an ensemble of optically trapped nanodiamonds. The arrow marks the NV zero phonon line. The spectrum of the phonon sideband is attenuated for wavelengths longer than 700 nm due to a dichroic optical filter that reflects the trapping laser into the objective. These nanodiamonds are not irradiated. The photographic inset shows this nanodiamond ensemble in the optical trap.

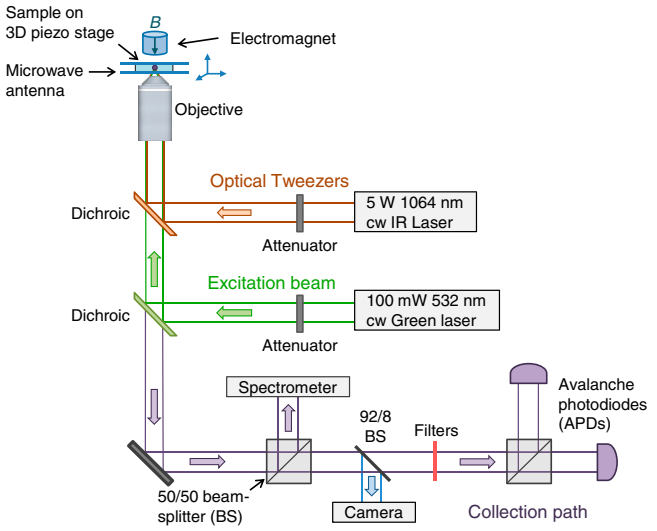


**Fig. S3.** The apparatus, with an optical tweezers path, an excitation beam path, and a collection path. All three optical paths are adjusted to the sample focus at the sample so that the photoluminescence signal is collected from the same confocal region where the nanodiamonds are trapped. During measurements, the trapping location remains fixed while a three-axis piezoelectric stage controls the sample position.

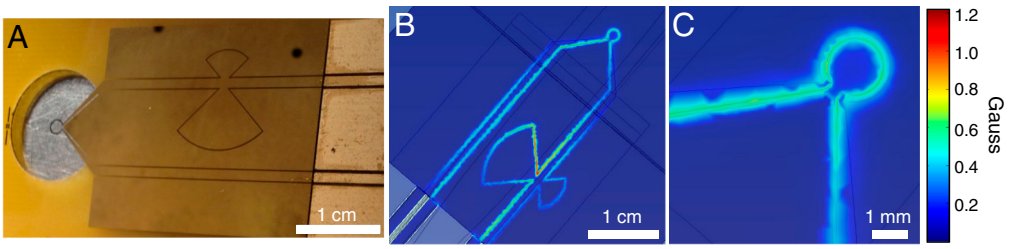


**Fig. S4.** (*A*) Photograph of the antenna/coverslip assembly. The hole in the antenna mount under the antenna loop permits optical access. (*B* and *C*) Magnetic flux density norm in the plane of the patterned antenna when $f_{MW} = 2.8$ GHz, modeled in COMSOL Multiphysics. Irregularities in the simulated magnetic flux density norm, appearing as splotching near the antenna trace edges, are an artifact of the chosen finite element meshing.

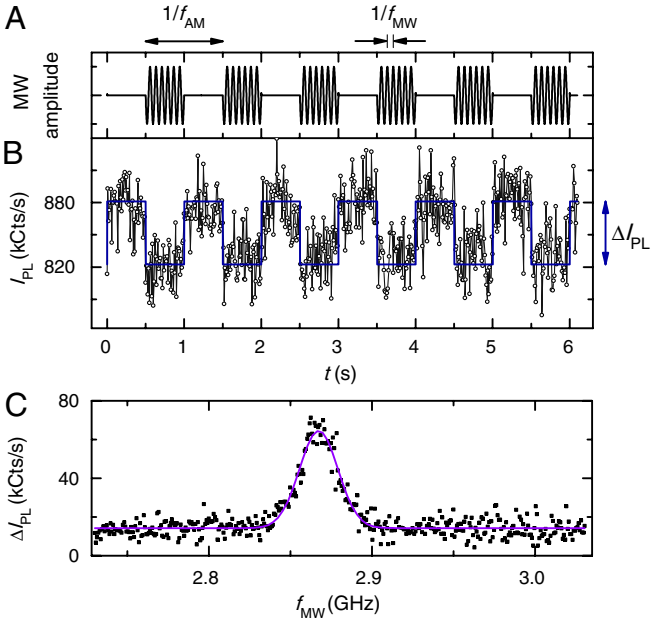


**Fig. S5.** Amplitude-modulated ESR of NV centers in optically trapped nanodiamonds in water. These nanodiamonds are irradiated. (*A*) Schematic of the amplitude-modulated microwave signal used in the experiments, with $f_{MW}$ lowered for illustration. (*B*) The readout contrast of the fluorescence signal created by the modulation amplitude of resonant, $f_{MW} = 2.868$ GHz, microwaves, modulated at frequency $f_{AM} = 1$ Hz. We use a software lock-in (blue line) to extract the differential fluorescence intensity $\Delta I_{PL} = 58.5$ kCts/s or the relative ESR signal $\Delta I_{PL}/I_{PL} = 6.64\%$. (*C*) Optically detected ESR spectrum obtained by sweeping $f_{MW}$ while $f_{AM} = 1$ kHz. The Gaussian fit (purple line) has a FWHM of 27.8 MHz and a peak at 2.87 GHz, which is the zero-field splitting between the $m_s = 0$ and the $m_s = \pm 1$ levels. This ESR spectrum was collected in 150 s. The bandwidth of the software lock-in is approximately 1 to 10 Hz.

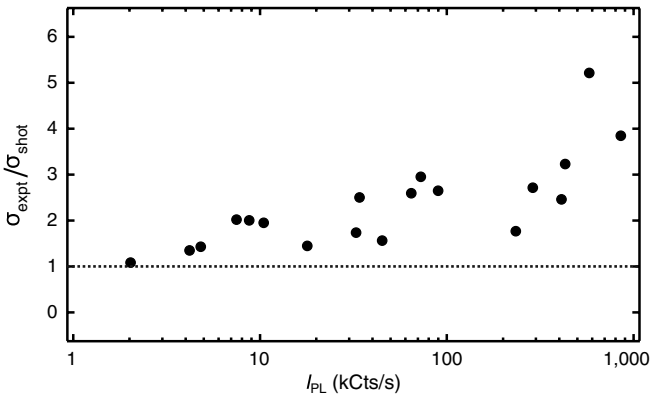


**Fig. S6.** The ratio of the measured standard deviation of $I_{PL}$ to shot noise obtained from total counts in a time interval $\Delta t$, $\sigma_{shot} = \sqrt{I_{PL}}\Delta t$, as a function of $I_{PL}$. The dotted line corresponds to the case when the measured noise equals the shot noise. This illustrates the increase in overall photoluminescence noise observed as the optical trap becomes more populated with fluorescent nanodiamonds.

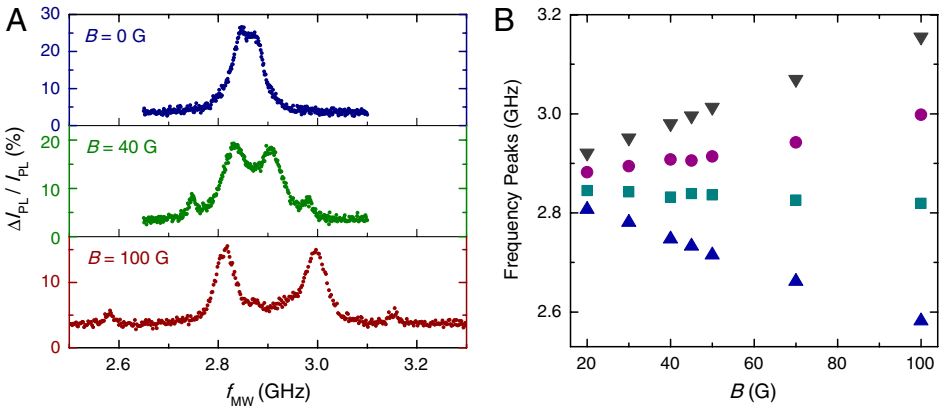


**Fig. S7.** (*A*) Optically detected ESR of dry nanodiamonds drop-cast and dried on a coverslip near a microwave antenna. These nanodiamonds are not irradiated. While a single spin will split into two peaks, here we observe at least four peaks, which indicate we are measuring multiple NV centers at different orientation with respect to the applied magnetic field. The frequency peaks of these ESR spectra are plotted in (*B*) as they vary with magnetic field.

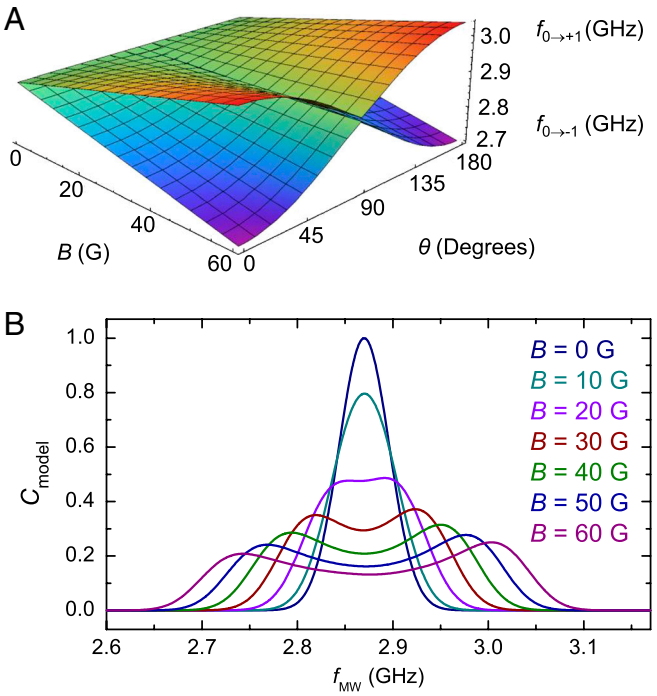


**Fig. S8.** (*A*) The spin sublevel transition frequencies $f_{0\to-1}$ and $f_{0\to+1}$ depend on both the magnitude $B$ of the magnetic field and the angle $\theta$ between the NV symmetry axis and the magnetic field vector. Here we assume the zero-field splitting is $D = 2.87$ GHz. (*B*) Modeled ESR spectra for an ensemble of randomly oriented NV centers, calculated from Eq. **S4**, and plotted with a zero-field width of 61.7 MHz and $D = 2.87$ GHz. These curves are also plotted as a colormap in Fig. 4*C*.

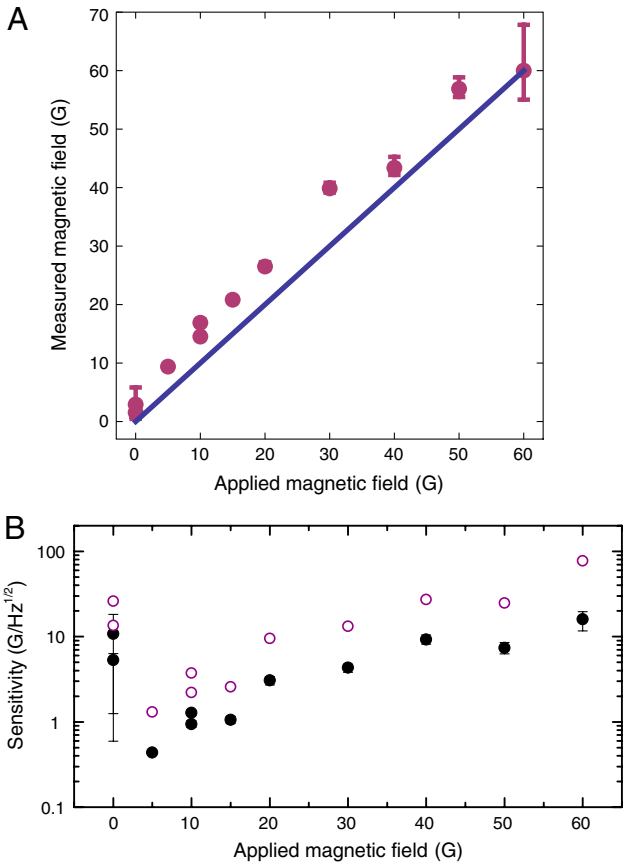


**Fig. S9.** (*A*) Magnetic field measured by the trapped NV ensemble versus applied magnetic field. Plotted error bars are 95% highest probability density intervals. The measured values are inferred from the model fitting while the applied values are set by an *ex situ* calibration. The solid line of unit slope and zero offset is used to compare the data against the ideal measurement. (*B*) The optimum sensitivity (black circles with error bars) and the demonstrated sensitivity (open purple circles) of the optically trapped nanodiamond-ensemble magnetometer.

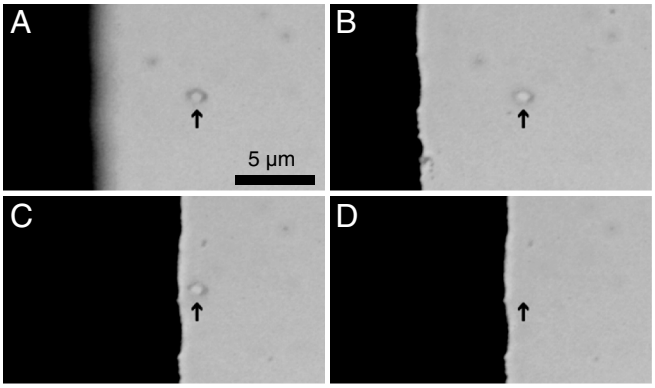


**Movie S1.** Spatial control of optically trapped nanodiamonds near the (black) microwave antenna (individual frames from movie, enhanced online). (*A–B*) The antenna is brought into focus, moving axially by 4.2 μm with respect to the trapped nanodiamonds from *A* to *B*. An arrow indicates the position of the optical trap, with nanodiamonds visible in both frames. (*C*) The antenna is moved laterally by 8.75 μm while the nanodiamonds remain trapped. (*D*) The trapping laser is blocked, releasing the nanodiamonds and allowing Brownian motion to scatter them away from the focus.

Movie S1(MOV)